Astron. Astrophys. 337, 223–232 (1998)

ASTRONOMY AND ASTROPHYSICS

Inference of steady stellar wind $v(r)$ laws from optically thin emission lines

III. Inversion of total line intensity distributions

R. Ignace[1], **J.C. Brown**[1], **J.E. Milne**[1], **and J.P. Cassinelli**[2]

[1] Department of Physics and Astronomy, University of Glasgow, Glasgow, UK
[2] Department of Astronomy, University of Wisconsin-Madison, USA

Received 26 February 1998 / Accepted 15 May 1998

Abstract. The variation with wavelength for a sequence of total intensities of stellar wind lines is considered as a basis for deriving the wind velocity law $v(r)$. In particular, we focus on the case where the continuum formation in the wind is dominated by the free-free opacity so that the inner radius increases with wavelength, as is realized in some massive winds like those of the Wolf-Rayet stars. The line emission in the wind occurs exterior to the continuum photosphere, hence lines observed at different wavelengths probe different regions of the wind acceleration. A major consequence of these physical conditions is the opportunity to infer $v(r)$, even if non-monotonic. Numerical examples are given to test the method, in which smooth and non-smooth monotonic $v(r)$, non-monotonic $v(r)$, and the effects of noise are addressed. In the absence of noise, the inversion of the simulated data for radius $r(\lambda)$ and expansion velocity $v(\lambda)$ is excellent. Even with noise at the 15% level, the recovery for $r(\lambda)$ remains reasonably robust, though the results for $v(\lambda)$ are more strongly affected. Although more sophisticated techniques are required to infer $v(\lambda)$ from noisy data, the simpler considerations presented here provide a basic theoretical framework for applying the inversion and indicate the potential of the method for deriving the wind flow structure.

Key words: line: profiles – stars: early-type – stars: mass-loss – stars: Wolf-Rayet

1. Introduction

In this paper multi-line spectral observations are considered as a means of deriving wind velocity distributions in dense stellar winds. We develop a technique to take advantage of the fact that the inner boundary radius of continuum formation in dense, hot stellar winds grows with increasing wavelength when the opacity is primarily free-free. Consequently, lines at different wavelengths sample different parts of the wind velocity distribution, a property that can be used to infer the velocity law from the line measurements. The situation is particularly relevant to the massive Wolf-Rayet (WR) winds.

The use of wind broadened emission lines and continua, particularly at the IR and radio wavelengths, as diagnostics of the wind density structure in early type stars has been investigated by numerous authors (Wright & Barlow 1975; Hartmann & Cassinelli 1977; Hillier et al. 1983; Bertout et al. 1985; Leitherer 1988; Morris et al. 1993, Puls et al. 1996). However, all of these methods rely on some parametrization for the wind velocity distribution, most commonly taken as a standard β-law based on the predictions of line-driven wind theory (Castor et al. 1975; Friend & Abbott 1986; Pauldrach et al. 1986). In the context of the WR stars, only Cannon (1974) considered inversion techniques for individual emission lines to derive the radial distribution of density, temperature, and velocity. However, even his method assumed power law distributions, and the effects of both absorption and occultation were neglected.

Brown et al. (1997; hereafter BRCI) have developed a more general inversion technique for deriving the wind velocity law from a single emission line profile. The assumptions of a steady spherical wind and optically thin emission lines are required to obtain an analytic expression for the inversion. As compared to Cannon (1974), the method of BRCI is more restrictive in that the wind is assumed isothermal, yet more general in that the velocity law is completely determined by the emission line profile without having to invoke parametric power law distributions. Ignace et al. (1998; hereafter IBRC) extended the formalism of BRCI to include the geometrical effects of stellar occultation for inverting the red wing of the profile.

Numerically, the method developed by BRCI and IBRC (a) works well, (b) is reasonably stable against noise, and (c) can yield a good recovery of any monotonic form of $v(r)$, provided that the distance scale in the problem can be estimated (this depends on the stellar mass loss rate $\dot{M}$ and the stellar distance D). Given their simplifying assumptions, the main limitation on the single line profile technique is that it applies to monotonic $v(r)$ distributions only. If the wind $v(r)$ is not in fact monotonic, the inversion method recovers that monotonic $v(r)$ which would produce the *same* line profile as observed (see Figs. 1 and 2

Send offprint requests to: R. Ignace

of BRCI). The fundamental reason for this ambiguity is that all parts $\Delta\lambda$ of a single line profile $F_{\lambda_0}(\Delta\lambda)$ sample the entire range of r (namely radii extending from R_0 to infinity, where R_0 is the photospheric radius at wavelength λ_0) and because the wind is optically thin, different ranges of v in the wind can be interchanged in radius without changing the profile $F_{\lambda_0}(\Delta\lambda)$, because every photon produced in the wind escapes the envelope.

One feature lacking from these different approaches to the inversion for $v(r)$ is the information gained from the combined use of both the continuum and line measurements. In this paper we take a first step toward the development of an inversion based algorithm that does combine these interrelated aspects of wind emission from early-type stars. Most of the same assumptions remain as in previous works, including spherical symmetry, isothermality, and homogeneity. However, we introduce a further data variable that allows sampling of different ranges of r to recover the wind velocity distribution even in the case of non-monotonic $v(r)$. This additional sampling yields a monotonic sequence of velocity ranges, and associated $v(r)$ values, so that the sign of the derivative $v'(r)$ can be determined in each range. In the absence of imaging, the only way to acquire such data is to observe multiple spectral lines of different rest wavelengths $\lambda_{\rm j}$ such that the photospheric radius $R_{\rm j}$ of the jth line varies with wavelength. In the present paper, we restrict ourselves to data of limited resolution giving only the total intensities of lines. Sect. 2 describes the theory of our line intensity inversion. Sect. 3 presents numerical simulations in which the method is tested against smooth and discontinuous monotonic velocity laws, non-monotonic velocity laws, and input data with noise. The final section presents a summary of the work with a discussion of future improvements in the technique.

2. Inversion of total line intensity distributions

We begin first by considering the emission arising from a single recombination line formed in a stellar wind and then discuss the continuum formation in the wind. Using both the line emission and a condition for the wind optical depth of the continuum, we present a derivation for inverting a distribution of line intensities to obtain $v(r)$.

2.1. The line emission

Following BRCI, we take the total emissivity (W m^{-3}) for the jth recombination line of wavelength $\lambda_{\rm j}$ to be $n_{\rm e}^2(r) f_{\rm j}(T)$ at radial distance r, and assume the wind temperature T to be constant. The factor $f_{\rm j}$ is $f_0(T,\lambda_{\rm j})$ in the notation of BCRI. Although not dependent on position in the wind (for constant T), the value of $f_{\rm j}$ does vary from line to line, being a factor that relates to the recombination coefficient associated with the jth line and to the appropriate elemental abundance. The wind electron density $n_{\rm e}(r)$ is given by the continuity equation in a spherical wind for a specified mass loss rate $\dot{M}$ and mean molecular weight per free electron $\mu_{\rm e}$:

$$n_{\rm e}(r) = \frac{\dot{M}}{4\pi\, r^2\, \mu_{\rm e}\, m_{\rm H}\, v(r)} \tag{1}$$

The total line intensity $F_{\rm j}^l$ (W m^{-2}) at the Earth a distance D from the source is

$$F_{\rm j}^l = \frac{\dot{M}^2\, f_{\rm j}}{64\pi^3\, \mu_{\rm e}^2\, m_{\rm H}^2\, D^2} \int_{V_{\rm j}} \frac{dV}{r^4\, v^2(r)}, \tag{2}$$

where $V_{\rm j}$ is the wind volume visible to the observer at wavelength $\lambda_{\rm j}$. This varies with j because the inner radius boundary in (2) is the photosphere $R_{\rm j} = R(\lambda_{\rm j})$ that is set by the free-free opacity (see Sect. 2.2). The line flux $F_{\rm j}^l$ is approximated as arising exterior to both the spherical volume of radius $R_{\rm j}$ and the occulted cylinder, also radius $R_{\rm j}$, behind the star. Expressing the differential volume element in spherical coordinates readily leads to the expression

$$F_{\rm j}^l = \frac{\dot{M}^2\, f_{\rm j}}{32\pi^2\, \mu_{\rm e}^2\, m_{\rm H}^2\, D^2} \int_{R_{\rm j}}^{\infty} \frac{dr}{r^2\, v^2(r)} \left[1 + \sqrt{1 - \frac{R_{\rm j}^2}{r^2}}\right], \tag{3}$$

where the terms inside the brackets ensure that only emission exterior to the occulting tube contribute to the observed line flux.

To make the expressions more managable, it is convenient here to introduce several normalizations. Defining $x = r/R_0$ for some convenient R_0 (independent of j), and $w(x) = v/v_\infty$ for wind terminal speed v_∞, we obtain

$$F_{\rm j}^l = \frac{\dot{M}^2\, f_{\rm j}}{32\pi^2\, \mu_{\rm e}^2\, m_{\rm H}^2 D^2\, R_0\, v_\infty^2} \int_{X_{\rm j}}^{\infty} \frac{dx}{x^2\, w^2(x)} \left[1 + \sqrt{1 - \frac{X_{\rm j}^2}{x^2}}\right], \tag{4}$$

where $X_{\rm j} = X(\lambda_{\rm j}) = R_{\rm j}/R_0$. Eq. (4) can be compactly rewritten as

$$F_{\rm j}^l = \frac{\lambda_{\rm j}\, v_\infty}{4\alpha_{\rm j}\, c} \int_{X_{\rm j}}^{\infty} \frac{dx}{x^2\, w^2(x)} \left[1 + \sqrt{1 - \frac{X_{\rm j}^2}{x^2}}\right], \tag{5}$$

where $\alpha_{\rm j} = 8\pi^2\, D^2\, \lambda_{\rm j}\, \mu_{\rm e}^2\, m_{\rm H}^2\, R_0\, v_\infty^3 / f_{\rm j}(T)\, \dot{M}^2\, c$ was introduced in IBRC and has units of (m^3 W^{-1}).

Adopting values for $\dot{M}/D$, R_0, and v_∞, we can express Eq. (5) solely in dimensionless variables

$$\begin{aligned} \Lambda_{\rm j} &= \frac{1}{2} \int_{X_{\rm j}}^{\infty} \frac{dx}{x^2\, w^2(x)} \left[1 + \sqrt{1 - \frac{X_{\rm j}^2}{x^2}}\right] \\ &= \frac{1}{2} \int_0^{Y_{\rm j}} \frac{dy}{w^2(y)} \left[1 + \sqrt{1 - \frac{y^2}{Y_{\rm j}^2}}\right], \end{aligned} \tag{6}$$

where $\Lambda_{\rm j} = F_{\rm j}^l/F_0$, $F_0 = \lambda_{\rm j}\, v_\infty/2\alpha_{\rm j}\, c$, $y = x^{-1}$, and $Y_{\rm j} = Y(\lambda_{\rm j}) = {X_{\rm j}}^{-1}$.

The two unknowns in (6) are $Y_{\rm j}$ and $w(y)$. If the values of $Y_{\rm j}$ for each observed line were known, then expression (6) could in principle be inverted to derive the wind velocity distribution. However the photospheric radius is defined by the condition that the continuum optical depth $\tau(\lambda_{\rm j})$ be of order unity at $y = Y_{\rm j}$. Therefore we must next consider the continuum formation process and the conditions that allow $Y_{\rm j}$ to be determined.

2.2. The continuum opacity

Assuming the dominant continuum opacity to be free-free and ignoring stimulated emission so that $h\nu/kT \equiv \lambda_{\rm Boltz}/\lambda \ll 1$, the opacity cross section at wavelength $\lambda_{\rm j}$ is given by $Q(\lambda_{\rm j}) = k_0^2 \lambda_{\rm j}^2 n_{\rm e}$, and hence the optical depth in the continuum at r is

$$\tau(\lambda_{\rm j}) \;=\; \int_r^\infty n_{\rm e}\, Q(\lambda_{\rm j})\, dr$$
$$\;=\; \left(\frac{\dot{M}\, k_0}{4\pi\, \mu_{\rm e}\, m_{\rm H}\, v_\infty}\right)^2 \frac{\lambda_{\rm j}^2}{R_0^3} \int_x^\infty \frac{dx}{x^4\, w^2(x)}. \qquad (7)$$

The constant k_0 is given by

$$k_0^2 = 1.78 \times 10^{-2}\, Z_{\rm i}^2\, g_\nu(T)\, c^2\, T^{-3/2}\, \frac{n_{\rm i}}{n_{\rm e}}, \qquad (8)$$

where $Z_{\rm i}$ is the root mean square charge per ion, $g_\nu(T)$ is the Gaunt factor (of order unity), and $n_{\rm i}/n_{\rm e}$ is the ratio of ion to electron number densities (Allen 1973). The slow variation of the Gaunt factor with wavelength will be ignored throughout the rest of our discussion. The optical depth unity condition is $\tau(\lambda_{\rm j}) = 1$, which upon substitution into (7) and some rearrangement gives

$$z_{\rm j}^{-2} = \left(\frac{\lambda_0}{\lambda_{\rm j}}\right)^2 = \int_{X_{\rm j}}^\infty \frac{dx}{x^4\, w^2(x)} = \int_0^{Y_{\rm j}} \frac{y^2\, dy}{w^2(y)}, \qquad (9)$$

where we have defined a convenient optical depth scale

$$\lambda_0 = \frac{4\pi\, \mu_{\rm e}\, m_{\rm H}\, v_\infty\, R_0^{3/2}}{\dot{M}\, k_0}. \qquad (10)$$

Values of λ_0 and $\lambda_{\rm Boltz}$ for several types of hot stars are listed in Table 1. Note that the subscripted numbers for T, $\dot{M}$, and v_∞ indicate powers-of-ten normalization. Small values of λ_0 correspond to more optically thick winds; large values indicate more optically thin winds. The parameter λ_0 is only a crude indicator of the continuum optical depth in the wind, because although it has a scaling like a mean free path, it fails to take the *slope* of $w(x)$ into account, which has consequence for the integral result of Eq. (9). Note that in deriving λ_0, the O star winds were assumed to be of completely ionized hydrogen and the WR stars of singly ionized helium.

Expression (9) relating the photospheric radius to wavelength is only valid for $\lambda_{\rm Boltz}/\lambda \ll 1$. From Table 1, the ratio $\lambda_{\rm Boltz}/\lambda$ is unity at UV wavelengths for the hot stars above 40,000 K and visible wavelengths for the cooler ones, so our approximation to the free-free opacity applies only at wavelengths significantly greater than $\lambda_{\rm Boltz}$. The results presented here will be applicable to IR and longer wavelengths of hot star spectra. In the next section, we take the integral equations (6) and (9) that involve the two unknowns $w(y)$ and $Y_{\rm j} = Y(\lambda_{\rm j})$ to formulate an inversion solution for a sequence of measured line intensities.

Table 1. Canonical Values of λ_0 and $\lambda_{\rm Boltz}$

Star	T_4 (K)	$\dot{M}_{-6}$ ($\rm M_\odot\ yr^{-1}$)	$v_{\infty,3}$ ($\rm km\ s^{-1}$)	R_* ($R_\odot$)	λ_0 (μm)	$\lambda_{\rm Boltz}$ (μm)
WC	6	50	2	5	6.9	0.24
WN	4	30	1.5	10	18.1	0.36
Of	4	10	3	20	76.7	0.36
O3	4	3	3.5	15	192	0.36
O9	3	1	2	10	146	0.48

2.3. Inversion of the line intensity distribution

In posing the inversion, it is more precise to say that (6) is an integral equation for the function $\psi(y) = w^{-2}(y)$ to be found by the inversion of the data $\Lambda(z_{\rm j}(Y))$ with kernel $K_{\rm j}(\xi = y/Y)$ given by

$$K_{\rm j}(\xi) = \frac{1}{2}\, \left[1 + \sqrt{1-\xi^2}\right]\, T(\xi), \qquad (11)$$

where T (not to be confused with temperature) is a top hat function, which is unity for $\xi \in [0,1]$ and zero for all other ξ. Since Λ is known as a function of $z_{\rm j}$ rather than of $Y(z_{\rm j})$, the integral equation has to be solved subject to condition (9) that defines $Y(z_{\rm j})$. Explicit analytic solution of this problem does not seem feasible, though it is straightforward if the occultation term is neglected (see below). Solution of this pair of equations could be carried out numerically for noisy data by any of the usual regularisation methods (Craig & Brown 1986). Henceforth in this paper we ignore the effects of stellar occultation to focus on what can be learned from analytic treatment of the equations when limited line profile data is available. In a subsequent paper, we plan to address the issue of occultation in conjunction with the problem of noise, for which initial considerations suggest certain advantages in the combined treatment.

We suppose now that the line is resolved sufficiently to enable separate measurement of the total fluxes $\Lambda_{\rm B}$ and $\Lambda_{\rm R}$ in the blueshifted and redshifted "halves" of the line profile, viz

$$\Lambda_{\rm j}^{\rm B} = \Lambda_{\rm B}(\lambda_{\rm j}) = \frac{1}{2} \int_0^{Y_{\rm j}} \frac{dy}{w^2(y)} - \Lambda_{\rm abs}^{\rm B} \qquad (12)$$

and

$$\Lambda_{\rm j}^{\rm R} = \Lambda_{\rm R}(\lambda_{\rm j}) = \frac{1}{2} \int_0^{Y_{\rm j}} \frac{dy}{w^2(y)}, \qquad (13)$$

where the occultation term has been deleted from Eq. (13). The term $\Lambda^{\rm B}_{\rm abs}$ represents the absorption profile owing to the intervening wind material along the line-of-sight to the star. We take the absorption profile as positive, being measured from zero flux (in contrast to the local continuum), and *subtract* it from the emission produced in the wind to get the final blueshifted profile. The absorption component present in $\Lambda_{\rm B}$ is a complication that is beyond the present theory, so the remainder of the paper concerns the more simple form of $\Lambda_{\rm R}$ only.

To obtain an inversion for $w(y)$, recall that the measured data consists of a series of line intensities with wavelength, $\Lambda_{\rm R}(z_{\rm j})$. Differentiating $\Lambda_{\rm R}$ by $z_{\rm j}$ in Eq. (13) yields

$$2\,\frac{{\rm d}\Lambda_{\rm R}}{{\rm d}z_{\rm j}} = \frac{1}{w^2(Y_{\rm j})}\frac{{\rm d}Y_{\rm j}}{{\rm d}z_{\rm j}}, \tag{14}$$

which shows that the changes in the normalized line intensities relate to both the wind velocity distribution and to changes in the photospheric radius. However, it is the continuum opacity that sets where the photosphere occurs as a function of wavelength. Differentiating the optical depth unity condition of Eq. (9) gives

$$2\,\frac{1}{z_{\rm j}^3} = -\frac{Y_{\rm j}^2}{w^2(Y_{\rm j})}\frac{{\rm d}Y_{\rm j}}{{\rm d}z_{\rm j}}. \tag{15}$$

Eliminating ${\rm d}Y_{\rm j}/{\rm d}z_{\rm j}$ between (14) and (15) provides the photospheric radius $Y_{\rm j}$ as a function of wavelength $z_{\rm j}$ in terms of the red flux gradient, viz

$$Y^2(z_{\rm j}) = -\,\frac{1}{z_{\rm j}^3}\left(\frac{{\rm d}\Lambda_{\rm R}}{dz_{\rm j}}\right)^{-1}. \tag{16}$$

With Eq. (16) for $Y_{\rm j}$ in terms of observables only, we may substitute back into either Eq. (14) or (15) to obtain the velocity distribution as a function of photospheric radius $w(Y_{\rm j})$, which of course is the same as inferring $w(y)$ at the points $y = Y_{\rm j}$ for all j. We choose to use Eq. (14):

$$w^2(Y_{\rm j}) \;=\; \frac{1}{2}\left(\frac{{\rm d}Y/{\rm d}z}{{\rm d}\Lambda_{\rm R}/{\rm d}z}\right)_{\rm j} \tag{17}$$

$$\;=\; \frac{1}{4z_{\rm j}^4\,Y_{\rm j}}\left(\frac{{\rm d}\Lambda_{\rm R}}{{\rm d}z_{\rm j}}\right)^{-2}\left[3 + z_{\rm j}\,\frac{{\rm d}^2\Lambda_{\rm R}/{\rm d}z_{\rm j}^2}{{\rm d}\Lambda_{\rm R}/{\rm d}z_{\rm j}}\right], \tag{18}$$

where the derivative $({\rm d}Y/{\rm d}z)_{\rm j}$ is straightforwardly evaluated from Eq. (16). In the following section, we employ the inversions of Eqs. (16) and (18) on a number of test cases.

3. Numerical examples

We begin first with a brief description of the cubic spline which we employ to evaluate the first and second derivatives of the input $\Lambda_{\rm R}(z_{\rm j})$ distributions. Then we discuss the results of the different numerical simulations.

3.1. The numerical method

For some function $u_{\rm i}$ known at points $t_{\rm i}$ for $i = 1, ..., N$, a cubic spline may be employed to either interpolate the known values onto a different grid of points or to evaluate derivatives at those points. The basis of the spline is that the second derivative $u''(t)$ be continuous and the first derivative $u'(t)$ be smooth. This means that u'' varies linearly between the points $u''_{\rm i}$ and $u''_{\rm i+1}$ and that u' is continuous across the boundary of the intervals $(t_{\rm j-1}, t_{\rm j})$ and $(t_{\rm j}, t_{\rm j+1})$. Following Press et al. (1994), a system of $N-2$ equations can be found for the N unknowns $u''_{\rm i}$ in terms of the knowns $t_{\rm i}$ and $u_{\rm i}$. The remaining two conditions required to close the system are assumptions on the values of either u' or u'' at the points $i = 1$ and $i = N$. The "natural spline" assumes $u''_1 = u''_{\rm N} = 0$, which is the case that we adopt.

There are two properties of the spline that can be used to our advantage in the numerical implementation of our inversion. The first is that, unlike central differencing schemes, the spline can output derivatives for input data that is arbitrarily spaced in the independent variable t. Emission lines that are unevenly spaced in wavelength is quite analogous to real observations, and so our test cases will be for model line intensities that are irregular in $z_{\rm j}$.

Second, we do have some prior knowledge of what to expect for the second derivative u'' in the context of our line distributions. The distribution $\Lambda_{\rm R}$ will crudely be like a power law in $z_{\rm j}$, thus nearly linear in the logarithm. Consequently, ${\rm d}\ln\Lambda_{\rm R}/{\rm d}\ln z_{\rm j}$ is nearly constant and ${\rm d}^2\ln\Lambda_{\rm R}/{\rm d}\ln {z_{\rm j}}^2 \sim 0$, so that for a logarithmic distribution of the line intensities, the natural spline will be an excellent approximation to the problem of consideration. Unfortunately, as detailed below, $\Lambda_{\rm R}$ approximates a power law in $z_{\rm j}$ only asymptotically as the wind speed approaches its terminal speed, corresponding to somewhat long wavelengths (anywhere between a few to tens of microns, depending on the specific velocity law), hence the natural spline will be least accurate at the lowest wavelength point but should be quite satisfactory at all other points.

It is useful here to note the relations between the first and second derivatives in $\Lambda_{\rm R}$ that are required for our inversion and those in the logarithmic distribution that are calculated with the spline. The first is the slope

$$m \equiv \frac{{\rm d}\ln\Lambda_{\rm R}}{{\rm d}\ln z_{\rm j}} = \frac{z_{\rm j}}{\Lambda_{\rm R}}\,{\Lambda_{\rm R}}', \tag{19}$$

which gives ${\Lambda_{\rm R}}'$ directly from cross-multiplication. A few mores steps are needed for the second derivative:

$$\frac{{\rm d}^2\ln\Lambda_{\rm R}}{{\rm d}\ln {z_{\rm j}}^2} \;=\; z_{\rm j}\,\frac{\rm d}{{\rm d}z_{\rm j}}\left(\frac{{\rm d}\ln\Lambda_{\rm R}}{{\rm d}\ln z_{\rm j}}\right) = z_{\rm j}\,\frac{\rm d}{{\rm d}z_{\rm j}}\left(\frac{z_{\rm j}}{\Lambda_{\rm R}}\,{\Lambda_{\rm R}}'\right)$$

$$\;=\; z_{\rm j}\left[\frac{{\Lambda_{\rm R}}'}{\Lambda_{\rm R}} - \frac{z_{\rm j}}{{\Lambda_{\rm R}}^2}\,({\Lambda_{\rm R}}')^2 + \frac{z_{\rm j}}{\Lambda_{\rm R}}\,{\Lambda_{\rm R}}''\right]$$

$$\;=\; m\left[1 - m + \frac{z_{\rm j}\,{\Lambda_{\rm R}}''}{{\Lambda_{\rm R}}'}\right]. \tag{20}$$

Again, taking the last line in this series of expressions combined with (19) for the slope m, one can straightforwardly solve for

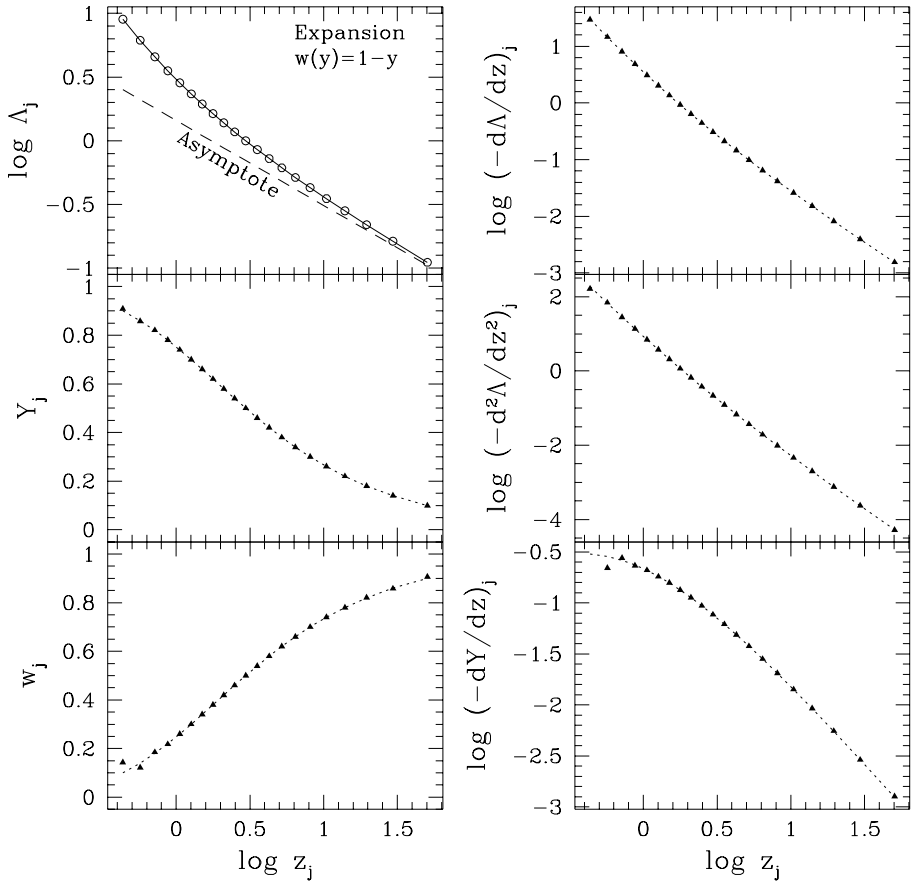

Fig. 1. This first figure shows the results of our inversion as applied to a simulated distribution of line intensities. For the velocity law we take $\beta = 1$. The upper left panel shows the input data (open circles), with the dashed line being the asymptotic distribution for a constant expansion wind. The middle and lower left panels contrast the recovered Y_j and w_j values (triangles) with the input (dotted line). Similarly, the right column displays the various derivatives required for the inversion. Our inversion is seen to reproduce the input with high accuracy.

Table 2. Summary of test cases

Figure	β	w_0	Npts	$y_{\min}$	$y_{\max}$	Noise(%)
1	1	0	21	0.1	0.9	0
2a	1	0	6	0.1	0.9	0
2b	1	0	6	0.2	0.4	0
2c	1/2	0	6	0.1	0.9	0
2d	–	–	18	0.1	0.9	0
3	–	–	23	0.1	0.9	0
4	1	0	6	0.1	0.5	5
5	1	0	6	0.1	0.5	15

$\Lambda_R{}''$ in terms $\mathrm{d}^2 \ln \Lambda_R / \mathrm{d} \ln z_j{}^2$ that is returned by the spline. We have written a computer code to simulate line intensity distributions and to evaluate the cubic spline to perform the inversion for the radius and velocity with wavelength. The code has been applied to a several test cases, that are described next.

3.2. Results from the numerical tests

Table 2 summarizes the different test cases relating the figure plots of the inversion results to the input parameters. Note that many of our examples employ the standard β velocity law for $w(y)$ given by

$$w(y) = w_0 + (1 - w_0)(1 - y)^\beta, \tag{21}$$

where w_0 is the initial wind speed at the lower boundary where $y = 0$. Although our current understanding of the line-driven winds of hot stars indicates that the radiative line force is intrinsically unstable (Owocki et al. 1988), the numerical simulations of the wind flow suggest that an average velocity distribution roughly described by a β-law is valid (Groenewegen & Lamers 1989). It is for this reason that we have selected a rather "smooth" parametrization of the wind velocity for our examples. Note, however, that we also consider a case where the velocity is non-monotonic.

Before describing the results of our tests, it is useful first to review the simple case of constant wind expansion. Returning to Eqs. (6) and (9), the normalized line intensity will scale as $\Lambda_R \propto X_j^{-1}$, and the radius of continuum formation will go as $X_j \propto z_j^{2/3}$. Combining we see that $\Lambda_R \propto z_j^{-2/3}$, with the consequence that $\mathrm{d} \ln \Lambda_R / \mathrm{d} \ln z_j = constant$ and $\mathrm{d}^2 \ln \Lambda_R / \mathrm{d} \ln z_j{}^2 = 0$. As will be discussed, these results for the case of constant expansion have relevance to the practical implementation of our inversion method.

3.2.1. Inversion for the monotonic case

The results of our first test are given in Fig. 1. Shown are six panels with the input line intensity distribution $\Lambda_R(z_j)$ (upper left), the recovered radii of continuum formation Y_j (middle left), the recovered velocities $w_j = w(Y_j)$ (lower left), and the

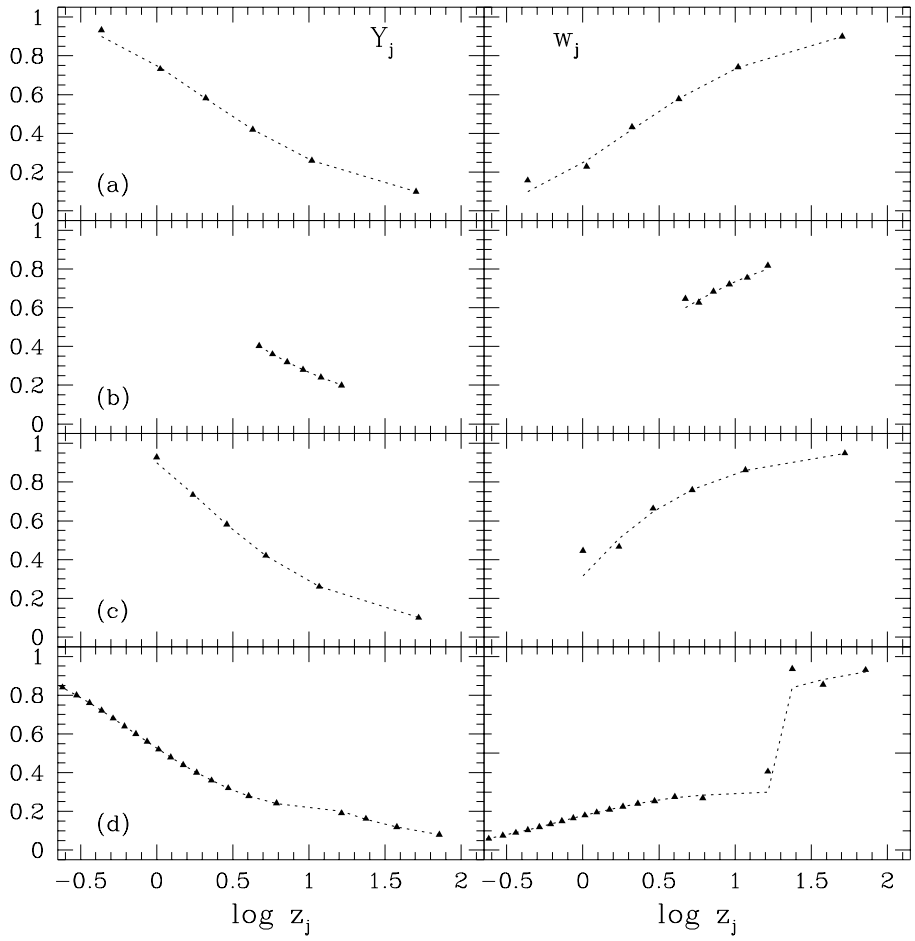

Fig. 2a–d. Shown are the results of our inversion as applied to four different cases. The $Y_{\rm j}$ values are left and the $w_{\rm j}$ values right. As in the previous figure, triangles are the recovered points; dotted lines represent the input. Case **a** is the same as Fig. 1 but for far fewer points. Case **b** is like **a** but for a much restricted region of input wavelengths. Case **c** is like **a** but for a $\beta = 1/2$ velocity law instead of $\beta = 1$. Case **d** shows how our inversion fairs for a monotonic wind expansion with a discontinuous jump in speed. Except for the lowest wavelength point, which being an endpoint is expected to have difficulties, our inversion recovers the flow structure with high accuracy. Even the jump in case **d** is recovered reasonably well.

various derivatives of the input data set that were used in the inversion (right column). As indicated in Table 2, a $\beta = 1$ velocity law was assumed with $w_0 = 0$. There are 21 points (20 intervals) in the input data set. These points are equally spaced in the input $Y_{\rm j}$ from $y_{\rm min} = 0.1$ ($x_{\rm max} = 10$) up to $y_{\rm max} = 0.9$ ($x_{\rm min} = 1.11$). The wavelength coordinate $z_{\rm j}$ is therefore unequally spaced.

The recovery (triangles) of the true distributions (dashed line) is impressive. Only near the endpoints, where difficulties can naturally be expected, do the recovered values deviate more than 1% from the input. Actually, for $Y_{\rm j}$ it is only the leftmost point that is discrepant at the 1% level; for $w_{\rm j}$ it is the first few points that are significantly off, somewhat worse owing to its dependence on the *second* derivative.

For our first test the input data set was purposely contrived, in that it is noiseless, contains a large number of points with a large dynamic range, and spans a considerable range in both radius and velocity. The test illustrates the following aspects of the inversion. (a) It demonstrates that our code is indeed operating properly, being able to recover in detail what was input. (b) For any reasonably smoothly varying function of $w(y)$, the resulting distribution of $\Lambda_{\rm R}(z_{\rm j})$ is power law "like". Hence, the various derivative quantities ($\mathrm{d}\Lambda_{\rm R}/\mathrm{d}z_{\rm j}$, etc) will also be near power laws. (c) There is a lot to be gained from inspecting the distribution of $\log\Lambda_{\rm R}$ vs $\log z_{\rm j}$ before applying the inversion. It is clear that if this distribution does achieve a true power law of slope $-2/3$ (i.e., within the errors) in some wavelength interval, then the wind has obtained constant expansion between the radii corresponding to those wavelengths. Consequently, the first and second derivatives of $\Lambda_{\rm R}$ are known, as well as $\mathrm{d}y/\mathrm{d}z_{\rm j}$. Since the measured line intensities are generally expected to become weaker with increasing wavelength, the noise will become worse so that any attempt to invert the data may produce spurious results toward long wavelengths. It is gratifying therefore that as the measurements become noiser, the $\Lambda_{\rm R}(z_{\rm j})$ distribution is likely to approach a known asymptote. Our method for diagnosing the wind structure therefore has greatest value at the shorter wavelengths where the wind speed is significantly different from its terminal value.

Fig. 2a–d shows a broader variety of simulations. Four cases are given, as labelled (a) – (d), with the left column comparing the recovered $Y_{\rm j}$ (points) with the input (line) and the right column for $w_{\rm j}$. Fig. 2a is simply the case of Fig. 1 but with only 6 points (5 intervals). It is evident that at least a few points are necessary for the method to have any value, since the calculation of second derivatives is required, yet even with just half a dozen, the accuracy of the recovery is quite high, granted difficulties at the endpoints. Fig. 2b is like 2a with the same velocity law and the same number of input points, but now spread over a much smaller range in wavelength. Again, the recovery is quite good.

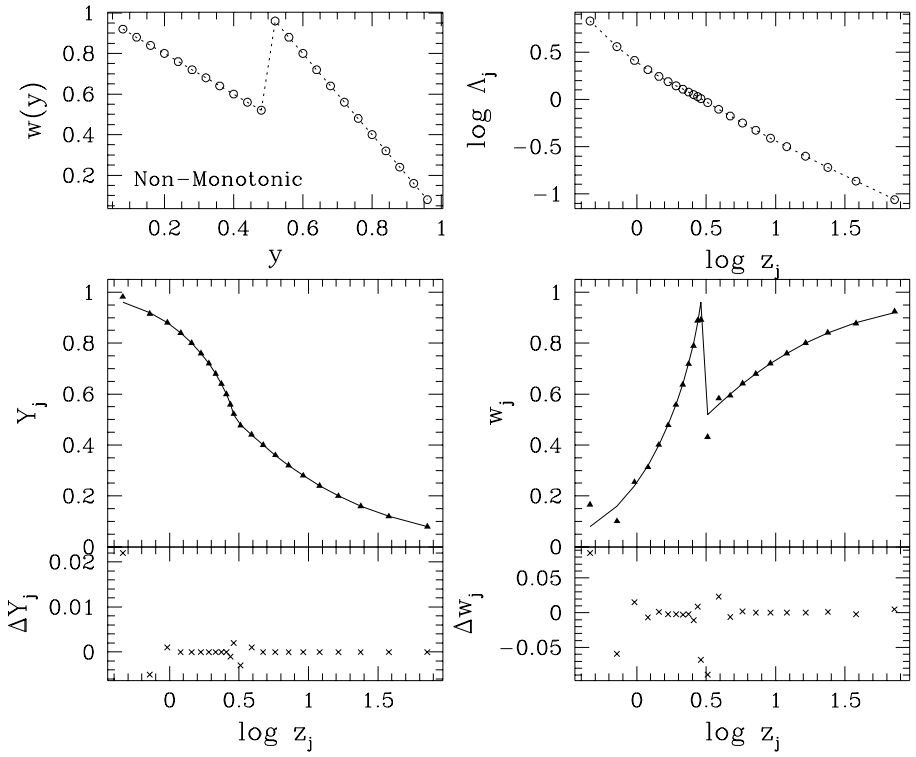

Fig. 3. Here our inversion is applied to another velocity law with a discontinuous jump, this time with $w(y)$ non-monotonic. The input distributions are shown at the top (circles). As in previous figures, the recovery is shown as triangles in the middle panels. The two lowest panels indicate the residuals between input and recovered as crosses. The inversion for $Y_{\rm j}$ is remarkably good; that for $w_{\rm j}$ is slightly less so, yet the discontinuity is well-resolved and there are regions where $w_{\rm j}$ is indeed recovered to high accuracy.

Case c is for a $\beta = 0.5$ velocity law with $w_0 = 0$. Inasmuch as $w(y)$ is smooth, changing the velocity law has little effect on the method's accuracy.

Fig. 2d is a significant variation of the previous cases. As can be seen from the input velocity, $w(y)$ is monotonic increasing, but discontinuous at $y = 0.2$ ($x = 5$) where w jumps from 0.3 up to 0.8. The recovery of the $Y_{\rm j}$ values is largely insensitive to the velocity jump. In contrast, the inversion struggles more to recover $w_{\rm j}$ in the vicinity of the jump. However, away from the discontinuity, as little as two or even just one point away, the method has accurately recovered the velocity distribution. The lesson here is that with a sufficiently large dataset, one or two bad points, be they extremely noisy or a true discontinuity in $w(y)$, will not in general corrupt the recovery of the velocity at other points, because the inversion at any given point depends primarily on its nearest neighbors. As with any treatment of data, there is little hope for accurately inverting a data set of poor quality, but an overall good data set with only a few bad measurements can still be expected to yield useful information on the wind flow structure.

3.2.2. Inversion for the non-monotonic case

In contrast to the discontinuous but monotonic case of Fig. 2d, Fig. 3 shows the inversion as applied to a discontinuous and non-monotonic radial wind speed. The upper two panels show the input $w(y)$ and $\Lambda_{\rm R}(z_{\rm j})$, with circles denoting the actual input. The velocity is linear in y on either side of the discontinuity with a drop from 1.0 to 0.5 at $y = 0.5$ ($x = 2.0$). The results of the inversion for $Y_{\rm j}$ and $w_{\rm j}$ are shown in the middle panels (points are the inversion; solid line follows the input). The residuals of the recovery $\Delta Y_{\rm j}$ and $\Delta w_{\rm j}$ are given as scatter plots at bottom. Ignoring endpoints, the recovery of $Y_{\rm j}$ is much better than 1%, and the same is true of $w_{\rm j}$ for the majority of points. The inversion resolves the non-monotonic discontinuity in $w_{\rm j}$ at the 5-10% level, similar to the discontinuous but monotonic case of Fig. 2d. So, as discussed previously, our inversion handles the non-monotonic cases just as well as monotonic and also does remarkably well when velocity discontinuities are present. The primary reason for the robustness of the technique is that in the absence of noise, the $\Lambda_{\rm R}$ distribution with wavelength is always monotonic, regardless of non-monotonicity and discontinuities in the wind velocity. However, the presence of noise can have a drastic effect on the results if no regularization is applied, a topic that we explore next.

3.2.3. Inversion for the case of noisy data

Figs. 4 and 5 demonstrate the effects of noise on the results of the inversion. The input is similar to that of Fig. 1 with a $\beta = 1$ and $w_0 = 0$ velocity law, but for only 6 points that evenly sample y between 0.1 and 0.5. The results are displayed in a similar format to that of Fig. 1, but with some detailed differences. The upper left panel shows the sum of $\Lambda_{\rm R}$ and noise as normalized to the true $\Lambda_{\rm R}$ without the noise. The recovery of $Y_{\rm j}$ and $w_{\rm j}$ are in the middle and lower left panels (points). The right column displays the various derivatives plotted in Fig. 1, but now as percentage differences from the actual values.

Gaussian noise was added to $\Lambda_{\rm R}$ such that a certain percentage noise (characterized by σ) was applied to the point with the highest $z_{\rm j}$ value, and this σ was held constant for the other points. Because σ is constant and $\Lambda_{\rm R}$ increases with decreas-

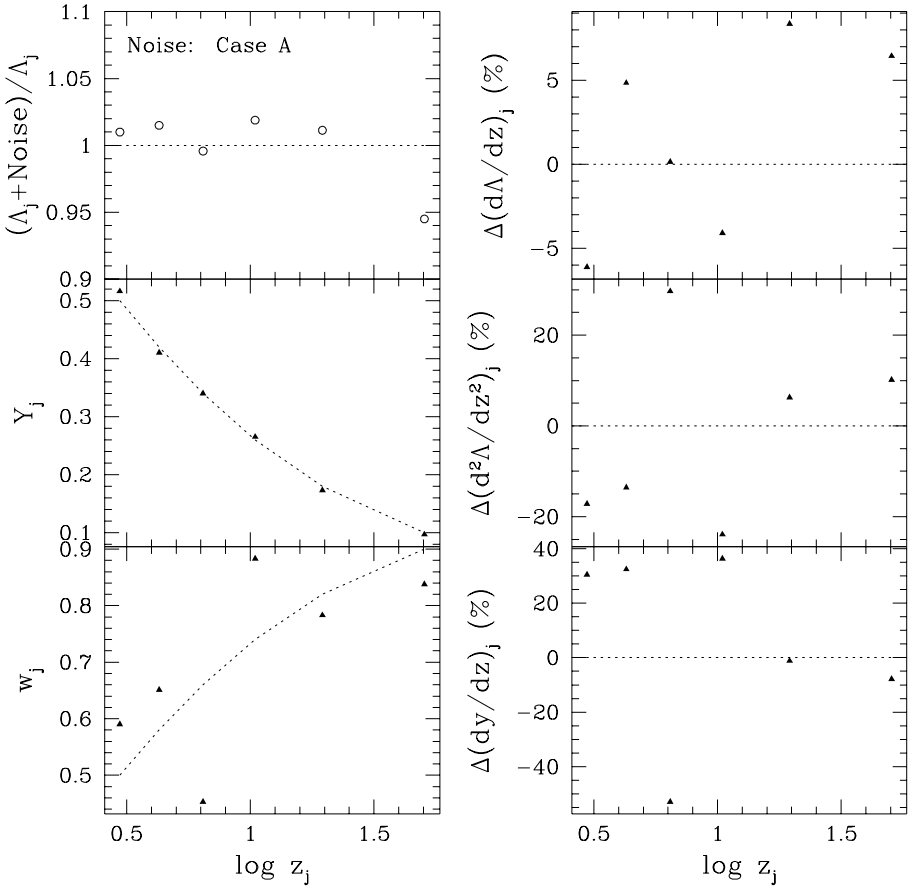

Fig. 4. This figure is similar to that of Fig. 1, only we have added noise to the input line intensities. The upper left panel now shows the *ratio* of $\Lambda_{\rm j}$ with noise to that without. As might be expected from real observations, the level of noise is higher for the typically weaker lines at longer wavelengths (i.e., larger $z_{\rm j}$ values). The noise level is 5% for the highest $z_{\rm j}$ point. The right column shows the percentage difference between the actual and recovered derivatives used in the inversion.

ing $z_{\rm j}$, the relative noise in the data likewise decreases with decreasing $z_{\rm j}$. The longer wavelength lines tend to be weaker than those at short wavelengths, hence this algorithm roughly simulates the relative noise levels that might be expected from real observations.

In the case of Fig. 4, noise at the 5% level was added to the final point. The recovery of $Y_{\rm j}$ is good to the 5% level; that of $w_{\rm j}$ is worse with errors up to about 20%, but the inversion for $w_{\rm j}$ does have the overall correct trend. The recovery for $Y_{\rm j}$ is quite good because it depends only on the square root of the first derivative $\mathrm{d}\Lambda_{\rm R}/\mathrm{d}z_{\rm j}$, so that the noise in $\Lambda_{\rm R}$ is somewhat suppressed in the inversion. However, $w_{\rm j}$ depends on both the first and second derivatives so that the noise is compounded.

Fig. 5 is like that of the previous case but with 15% noise in the last point. Again the recovery for $Y_{\rm j}$ is remarkably good at the 10% level. However, the inversion for $w_{\rm j}$ is extremely poor. Errors in the second derivative of $\Lambda_{\rm R}$ and the related quantity $\mathrm{d}y/\mathrm{d}z$ are approaching the 100% level, and no reasonable result can be expected without the aid of regularization.

4. Conclusions

This paper has presented a continuation of inversion approaches to deriving the flow properties of stellar winds from emission line observations. Whereas the two papers preceding this have concentrated on the information content available in a single highly resolved emission line profile, here we have focussed on what may be gained from considerations of low resolution multi-line observations, specifically in terms of the distribution of line intensities with wavelength. The major results of this study are (assuming spherically symmetric winds and ignoring the effects of occultation):

(a) Recovery of the radius of continuum formation $X_{\rm j}$ depends on the first derivative of the line intensity distribution with wavelength, whereas the speed of expansion at that radius depends on both the first and second derivatives. The inversion was used on several numerical test cases, and the results appear extremely promising.

(b) Unlike the individual profile considerations of BRCI and IBRC, the multiline approach is capable of recovering non-monotonic velocity laws as well as monotonic. The resolution of any non-monotonicity depends not only on the intrinsic properties of $w(x)$ but also on the wavelength interval between lines (i.e., the sampling interval). Poor wavelength coverage in lines will naturally result in a crude recovery of the wind flow structure so that signatures of non-monotonicity may be "washed-out" unless characterized by high amplitude changes in w or a non-monotonic velocity feature that is radially extended throughout the wind.

(c) A natural consequence of (a) above is that the recovery for $X_{\rm j}$ is much less sensitive to noise, depending only on the first derivative, than is $w_{\rm j}$, which requires also the second derivative. Thus, applications of regularization methods common

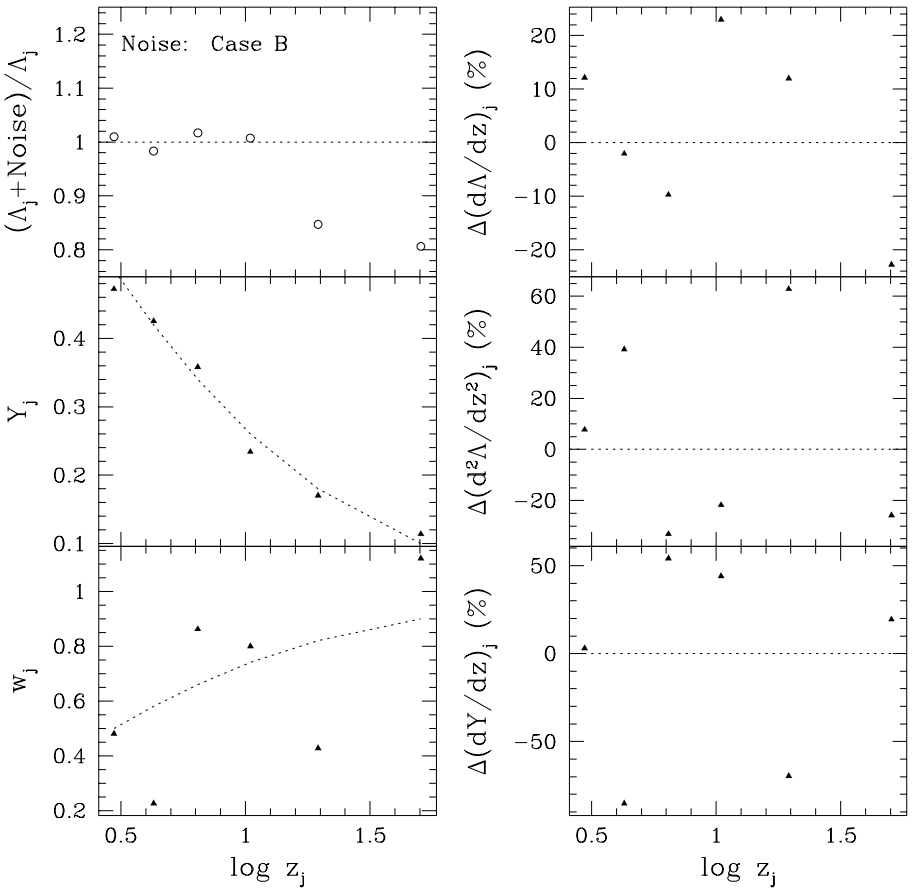

Fig. 5. This figure is as Fig. 4 but for a noise level of 15% at the highest z_j point. The inversion for Y_j is still quite good; that for w_j is almost completely spurious.

to most inversion problems will have to be considered in the future. Even so, for data where X_j can be recovered reliably but w_j is spurious, an estimate of w_j at X_j can be obtained from the FWHM of the line. Note that using the FWHM will likely give underestimates owing to the fact that occultation in the red wing and absorption in the blue wing will tend to narrow emission profiles.

(d) A drawback of the present method is the neglect of stellar occultation, which from IBRC is known to have a substantial effect on the results of the inversion. However, this work has emphasized explorations of a novel approach to probing the properties of winds, with particular applications to the massive winds of the Wolf-Rayet stars. In that spirit we have laid a foundation for attacking more sophisticated problems involving stellar occultation and inversion in the presence of noise, a topic that we plan to pursue in future work.

In applying the method to observations, the issues of spectral resolution and line selection must be addressed. In the former our inversion is well-suited to low resolution spectral lines, because the method depends only on the integrated line intensity (i.e., of the redshifted emission). Being an integrated property, the line intensity will have a higher signal-to-noise (S/N) than the specific intensity at any single frequency in the line itself. Hence the time required to achieve a given S/N for the line intensity will be shorter than for the same S/N of the specific intensity.

As regards line selection, our inversion has been derived for recombination lines only. Using our normalization for the line intensity, the inversion can be applied to lines of any ionic stage of any atomic species. Of course in the real analysis, care must be taken to choose unblended lines, or blended lines where the component of interest is known to dominate the emission. Additionally, there are advantages in selecting lines of the same ion (e.g., the n–5 Pfund series of HI or the n–8 series of HeII), as additional information can be gleaned on departures from LTE and isothermality, effects not included in our inversion. The constraints on such departures provide a level of confidence on applying the results of this work and accompanying assumptions to the data.

In the context of the Wolf-Rayet winds, for which our method is most directly applicable, we note that the inversion given here is somewhat less sensitive to the broadening effects of electron scattering than are the profile inversions of BRCI and IBRC. The latter inversions depend on the profile slope, for which electron scattering can have a major influence. In contrast, the line intensity method depends on the integrated line flux, so even though the electron scattering can significantly alter the profile shape, all of the line photons are conserved (Hillier 1991). However, electron scattering can redistribute blue photons into the red wing, and since we treat only the red wing, our method will be suspect in cases where the electron optical depth between the observer and the radius of continuum forma-

tion at wavelength $\lambda_{\rm j}$ much exceeds unity. As the continuum radius marches out into the wind with increasing wavelength, observations show that lines of lower ionization states become more prominent (e.g., Schulte-Ladbeck, Eenens, & Davis 1995). Hence recombination is efficient and there will be fewer electrons available to broaden the line, so the electron scattering effects should not significantly bias our method in this regime.

As a springboard to future investigations, there is an aspect of the current problem that is intimately linked to deriving an inversion for the case with occultation as described in point (d), namely the slope of the continuum emission. We combine the optical depth unity condition with an equation for the total line luminosity to get $X_{\rm j}$ and $w_{\rm j}$. Alternatively, we could have combined the optical depth expression with one for the continuum luminosity. We speculate that this third piece of information, the continuum distribution, will allow us to incorporate the geometrical effects of stellar occultation into our inversion technique.

Acknowledgements. This work was supported by UK PPARC Rolling, Visitor, and STARLINK grants (RI, JCB), by a Royal Society of Edinburgh Cormack Vacation Scholarship (JEM), and by an NSF Grant AST-9417186 to the University of Wisconsin (JPC).

References

Allen, C. W., 1973, Astrophysical Quantities (The Athlone Press)
Bertout C., Leitherer C., Stahl O., Wolf B., 1985, A&A 144, 87
Brown J. C., Richardson L. L., Cassinelli J. P., Ignace R. (BRCI), 1997, A&A 325, 677
Cannon C. J., 1974, A&A 34, 387
Castor J. I., Abbott D. C., Klein R. I., 1975, ApJ, 195, 157
Craig I. J. D., Brown J. C., 1986, Inverse Problems in Astronomy: A Guide to Inversion Strategies for Remotely Sensed Data (Bristol and Boston)
Friend D. B., Abbott D. C., 1986, ApJ 311, 701
Groenewegen M. A. T., Lamers H. J. G. L. M., 1989, A&A Supp. 79, 359
Hartmann L. W., Cassinelli J. P., 1977, ApJ 215, 155
Hillier D. J., 1991, A&A 247, 455
Hillier D. J., Jone T. J., Hyland A. R., 1983, ApJ 271, 221
Ignace R., Brown J. C., Richardson L. L., Cassinelli J. P. (IBRC), 1998, A&A, in press
Leitherer C., 1988, ApJ 326, 356
Morris P. W., Brownsberger K. R., Conti P. S., Massey P., Vacca W. D., 1993, ApJ 412, 324
Owocki S. P., Castor J. I., Rybicki G. B., 1988, ApJ 335, 914
Pauldrach A., Puls J., Kudritzki R. P., 1986, A&A 164, 86
Press W. H., Teukolsky S. A., Vetterling W. T., Flannery B. P., 1994, Numerical Recipes in C (Cambridge University Press)
Puls J., Kudritzki R.-P., Herrero A., et al., 1996, A&A 305, 171
Schulte-Ladbeck R. E., Eenens P. R. J., Davis K., 1995, ApJ 454, 917
Wright A. E., Barlow M. J., 1975, MNRAS 170, 41